PAPER

Physically-based simulation of elastic-plastic fusion of 3D bioprinted spheroids

IOP Publishing Biofabrication 15 (2023) 045021 https://doi.org/10.1088/1758-5090/acf2cb

Biofabrication

PAPER

Physically-based simulation of elastic-plastic fusion of 3D bioprinted spheroids

Hassan Bahrami[1,*], Federico Sichetti[2], Enrico Puppo[2], Laura Vettori[1], Clara Liu Chung Ming[1], Stuart Perry[1], Carmine Gentile[1] and Nico Pietroni[1]

[1] Faculty of Engineering and Information Technology, University of Technology Sydney, 15 Broadway, Ultimo NSW 2007, Australia
[2] Department of Computer Science, University of Genova, Genova, Italy
[*] Author to whom any correspondence should be addressed.

E-mail: hassan.bahrami@student.uts.edu.au

RECEIVED
10 May 2023

REVISED
10 August 2023

ACCEPTED FOR PUBLICATION
22 August 2023

PUBLISHED
15 September 2023

Keywords: 3D bioprinting, physically-based simulation, spheroid, elastic-plastic

Abstract

Spheroids are microtissues containing cells organized in a spherical shape whose diameter is usually less than a millimetre. Depending on the properties of the environment they are placed in, some nearby spheroids spontaneously fuse and generate a tissue. Given their potential to mimic features typical of body parts and their ability to assemble by fusing in permissive hydrogels, they have been used as building blocks to 3D bioprint human tissue parts. Parameters controlling the shape and size of a bioprinted tissue using fusing spheroid cultures include cell composition, hydrogel properties, and their relative initial position. Hence, simulating, anticipating, and then controlling the spheroid fusion process is essential to control the shape and size of the bioprinted tissue. This study presents the first physically-based framework to simulate the fusion process of bioprinted spheroids. The simulation is based on elastic-plastic solid and fluid continuum mechanics models. Both models use the 'smoothed particle hydrodynamics' method, which is based on discretizing the continuous medium into a finite number of particles and solving the differential equations related to the physical properties (e.g. Navier–Stokes equation) using a smoothing kernel function. To further investigate the effects of such parameters on spheroid shape and geometry, we performed sensitivity and morphological analysis to validate our simulations with *in-vitro* spheroids. Through our *in-silico* simulations by changing the aforementioned parameters, we show that the proposed models appropriately simulate the range of the elastic-plastic behaviours of *in-vitro* fusing spheroids to generate tissues of desired shapes and sizes. Altogether, this study presented a physically-based simulation that can provide a framework for monitoring and controlling the geometrical shape of spheroids, directly impacting future research using spheroids for tissue bioprinting.

1. Introduction

Increasing advancements in biomedical engineering and additive manufacturing led to the biofabrication of human tissues from cells [1–3]. In the body, cells grow, replicate and organize in complex tissues and organs to generate the human body [4, 5]. Recent research in biofabrication has enabled us to 3D bioprint cells in hydrogels to replicate human morphogenesis, potentially using them as replacement body parts for patients [6–12]. The capacity of 3D bioprinters to build tissues by depositing cellular material in specific locations has provided invaluable assistance in producing highly complex and diverse shapes and sizes, including the design of the bioink used in this process [13–17].

A common approach to promote tissue morphogenesis using cells is based on their ability to organize in spheroid cultures. Spheroids are aggregates of cells that can be used to model tissues and organs. For example, our team has developed cardiac spheroids to mimic the complex human heart microenvironment for *in-vitro* and *in-vivo* applications [6, 18, 19]. Spheroids can be used as building blocks to create

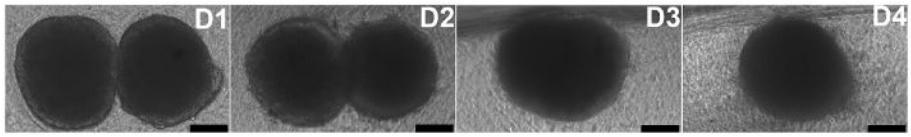

Figure 1. Fusion of bioprinted cardiac spheroids in alginate/gelatin hydrogels. Paired cardiac spheroids containing cardiac myocytes, endothelial and fibroblasts were bioprinted in 4% alginate/8%gelatin hydrogels and cultured for four days until complete fusion. Magnification bars equal 50 μm.

complex tissues when 3D bioprinted in tissue-tailored hydrogels due to their ability to fuse with each other [11, 20, 21]. They are embedded in biomaterials known as hydrogels [22].

Kim *et al* [22] found that the spatial arrangement of the spheroids within the hydrogels played a significant role in regulating spheroid fusion. Specifically, they observed that spheroids closely arranged in a hexagonal pattern showed a higher degree of fusion than those randomly distributed within the hydrogel. They attributed this to the increased contact area between the spheroids in the hexagonal pattern, which promoted fusion. Hence, the hydrogel's properties play a major role in spheroid fusion and can determine the size and shape of the bioprinted construct. Hydrogels can be made from different materials with different physical and chemical properties, affecting the final shape [23, 24]. Figure 1 shows microscopic images of a spheroid pair's spontaneous fusion.

A key challenge in bioprinting is to develop accurate models to predict and guide how spheroids replicate and merge to form complete tissues [25, 26]. Due to the lack of direct control over the fusion process, the final bioprinted tissue can have a significantly different shape than expected. Identifying the parameters that control spheroid fusion is essential to predict and fabricating a tissue with a desired shape and size. These parameters can include the hydrogel stiffness, spheroids density, and the distance between spheroids. We hypothesize that changing these parameters will affect the shape of the spheroids during the fusion. However, testing all possible parameter values is impractical due to the cost and time constraints. To address this constraint, we propose a simulation framework to model spheroid deformation during fusion. The simulation has its own parameters, allowing us to observe how spheroids behave under different conditions. Optimizing simulation parameters based on the desired shape of spheroids and doing reverse engineering can help scientists create tissue with the desired shape and save time and budget.

Simulation of the bioprinting process has the potential to significantly reduce experimental time and costs [27–29]. Therefore, this study focuses on developing a new computational and graphical framework for simulating spheroid fusion. The framework focuses on the physical and mechanical properties of fusing spheroids and allows us to replace classical trial-and-error methods. Our framework will enable us to predict the behaviour of spheroids during their fusion by tuning simulation parameters. This approach has not been used previously to model the spontaneous fusion process of spheroids.

The methodology described in this study employs and extends continuum mechanics models used in computer graphics to simulate elastic-plastic fluid, and elastic-plastic solid [30]. A common approach to solving the equation and approximating a continuous physical model is to sample the domain into particles. These particles sample different physical quantities over the volume, such as mass, velocity, and viscosity. This method is usually called smoothed particle hydrodynamics (SPH) [31]. Using particle-based systems, we have developed two types of continuum mechanics models:

- The first model considers spheroids as an elastic-plastic solid material, therefore containing elastic, plastic and volume conservation forces.
- The second model considers spheroids as an elastic-plastic fluid material, therefore containing elastic, plastic, viscosity and pressure forces.

Over the last two decades, the games and entertainment industries have extensively used physically-based simulation [32] to simulate rigid [33, 34] or deformable objects [32, 35–38]and also render realistic fluids [30, 39–44].

We adapted these techniques to simulate the behaviour of spheroids. To model elastic-plastic solid spheroids, we used the physically-based simulation based on SPH proposed by Mueller and colleagues [30]. Spatial derivatives are interpolated over volume using a moving least squares (MLS) procedure. We use these derivatives to obtain physical quantities such as stresses and elastic forces in the continuous. To model elastic-plastic fluid spheroids and derive numerical solutions, we use the well-established Navier–Stokes equations.

It is important to note that particles do not represent the cells inside the spheroids; instead, they are physical quantities. Our model's assumptions can be summarized as follows: (i) Spheroids are assumed to be symmetrical and spherical continuum media;

(ii) The particles in our models carry physical attributes such as mass, velocity, and acceleration; (iii) Spheroid fusion is assumed to be identical; (iv) In the solid-based model, spheroids are considered solid elastic-plastic materials; (v) In the fluid-based model, spheroids are modelled as incompressible fluids with elastic-plastic properties; (vi) Particles of a spheroid are attracted to the centre of mass of the other spheroid.

Although the specific biological mechanisms underlying spheroid fusion are complex, our observations indicate that the process involves a combination of short-range intermolecular potential forces and surface adhesion forces between the cells of adjacent spheroids upon contact. In our study, we have employed the Lennard-Jones potential to model the short-range attractive forces between spheroids [45]. It has various applications in different fields such as molecular dynamics and chemistry [46, 47].

Regarding the surface adhesion forces, we consider the role of integrins, which are transmembrane receptors involved in cell-cell and cell-matrix interactions. Integrins bind to extracellular matrix components, such as fibronectin, collagen, and laminin, through specific ligand-binding sites. These integrin-mediated adhesion forces can be modelled using various approaches [48, 49]. To simulate this behaviour, we establish connections between particles of different spheroids at the moment of contact. By doing so, we simulate the formation of elastic-plastic links between different particles of adjacent spheroids.

This combined approach allows us to capture the attractive forces between spheroids, incorporating both the short-range intermolecular potential forces described by the Lennard-Jones potential and the surface adhesion forces mediated by integrins. By considering these physical interactions, we aim to provide a comprehensive understanding of the fusion process and its underlying biophysical mechanisms.

In the material and method section, we will demonstrate the mathematical details of the proposed models and their implementation *in-silico*. Then we will validate the *in silico* results by designing, conducting *in-vitro* experiments and morphological analysis, and comparing the results with simulations.

The remainder of the report is structured as follows: section 2 outlines our methodology for addressing the problem and its *in-silico* implementation. We will present the results of the models and their *in-vitro* validation in section 3 and discuss the sensitivity and morphological analysis in section 4.

2. Methodology

To achieve our goals, we designed a method to physically simulate the fusion of spheroids after printing. Spheroid fusion is a biologically complex process involving many factors, some of which are not directly observable. First, we must know the appropriate mathematical model to describe their physical behaviours. As we specified in the introduction, we first implemented an elastic-plastic solid model based on Muller *et al* [30], and then we also developed an elastic-plastic fluid-based model with different fluid parameters. In the following sections,

we will provide the mathematical description of the solid (section 2.1) and fluid (section 2.2) models and their implementation (section 2.3).

2.1. Solid-based model

In this section, we assume that the spheroids are elastic-plastic solid materials. To describe their fusion process, we need to develop an elastic-plastic model that can explain the elasticity and plasticity of the spheroids during the fusion process. To better understand the dynamic behaviour of this system, we will use a continuum mechanics model based on Muller *et al* [30] in which the elastic and plastic behaviour of an object can be simulated using the SPH method. The main idea of the model is to use a Green-Saint-Venant strain tensor for each particle:

$$\varepsilon = \mathbf{J}^{\mathrm{T}}\mathbf{J} - \mathbf{I} = \nabla\mathbf{u} + \nabla\mathbf{u}^{\mathrm{T}} + \nabla\mathbf{u}\nabla\mathbf{u}^{\mathrm{T}}. \quad (1)$$

The equation (1) uses various matrices, such as $\mathbf{u}$ which represents a continuous displacement vector field, $\mathbf{I}$ is the identity matrix, and $\mathbf{J}$ is the Jacobian matrix of the deformed model. The term ε encompasses both elastic and plastic strain ($\varepsilon = \varepsilon^e + \varepsilon^p$). To extract the plastic strain ε^p from the total strain ε, we need to separate it from the elastic deformation strain ε^e. Initially, we assume plastic strain is zero, and the algorithm proposed by O'Brien *et al* [50] is employed to update the plastic strain value (See algorithm 2). Consequently, stress can be computed using Hooke's law:

$$\sigma = \mathbf{C}\varepsilon \quad (2)$$

where $\mathbf{C}$ is a rank four tensor, approximating the constitutive law of the material. After some mathematical manipulation, particle i's elastic force is equal to:

$$\mathbf{f_{ie}} = -\sigma\nabla\mathbf{u}_i\varepsilon. \quad (3)$$

Green's strain tensor in equation (1) will be zero for the volume inverting displacement field. Therefore, there will be no restoring volume inversion force. For this reason, a volume conservation force is needed to penalize deviations of the determinant of the Jacobian from the positive side. Hence, the volume energy term will be:

$$U_v = \frac{1}{2}k_v\left(|\mathbf{J}| - 1\right)^2 \quad (4)$$

where k_v is the volume constant. Consequently, the volume conservation force is equal to:

$$\mathbf{f_{iv}} = -\sigma\nabla\mathbf{u}_i U_v = -k_v\left(|\mathbf{J}| - 1\right)\sigma\nabla\mathbf{u}_i|\mathbf{J}|. \quad (5)$$

Therefore, the total internal force applied to the ith particle is equal to the sum of elastic and conservation forces:

$$F_i = f_{ie} + f_{iv}. \tag{6}$$

The MLSs method has been used to solve differential displacement equations to obtain the Jacobian matrix. In the next section, we will describe the details of our developed elastic-plastic fluid model.

2.2. Fluid-based model

The Navier–Stokes equation generally describes fluid dynamics. Navier and Stokes formulated this fluid mechanics equation, the basis for essentially all fluid mechanical works today. This paper will use the incompressible Navier–Stokes equation that governs fluids like water at normal velocities and temperatures. Other forms of these equations are compressible, generally used for supersonic and hypersonic phenomena, which can have shockwaves and discontinuities in the solution. However, in incompressible equations, such phenomena are not allowed. It is worth mentioning that all the everyday intuitions we have about how fluids work correspond to the behaviour of incompressible equations. Hence, the incompressible equations are the ones we consider for physically-based simulation. The general form of the Navier-Stocks equation is as follows:

$$\rho\left[\frac{\partial v}{\partial t} + v.\nabla v\right] = \rho g - \nabla p + \mu\nabla^2 v + F_{\text{elastic}-\text{plastic}}$$
$$\rho(\nabla \cdot v) = 0 \tag{7}$$

where ρ is density, p is pressure, g is gravity and v is velocity. $F_{\text{elastic}-\text{plastic}}$ is computed the same as in the solid-based model. Also, $v.\nabla v$ is convective acceleration. We can use the simplified equation of state to calculate the pressure, denoted by p [51]. Thus we have:

$$p = k(\rho - \rho_0) \tag{8}$$

where ρ_0 is the resting density, pressure and density are scalar variables, while gravity and velocity are vectors. k is the gas constant that depends on the temperature. From the right-hand side of the equation (7), we can find that the fluid moves under the force of gravity, pressure, and viscosity. We have convective acceleration from the left-hand side of the motion equation. We know that the gradient is the higher-dimension analog of slope in one dimension. Hence, the gradient of p is given by the partial derivatives of p with respect to x, y and z. It is important to note that the equation of motion is governed by a negative pressure gradient, indicating that the system moves in a downward direction along the pressure gradient. This implies that the system transitions from regions of higher pressure to regions of lower pressure according to its natural equations of motion. The pressure, denoted as p, is defined as the difference between the fluid density at a specific point and a reference value known as the 'resting density.'

The operator ∇^2 facilitates the diffusion of velocity, resulting in the dispersion of momentum across the system. In essence, this process leads the system to a state of uniform velocity throughout, driven by its inherent forces.

Also, there is a mass continuity equation in equation (7). In the case of the incompressible equations, it says that mass will be neither created nor destroyed.

2.3. Implementation

The basic idea of the SPH method is to discretize a continuous medium (in our case, a spheroid) to a finite number of particles and distribute the different particle attributes in its volume by using a kernel function (see figure 2). We remark here that particles are *not* meant to represent the cells that constitute the spheroid, as they merely provide a discrete version of the spheroid seen as a continuum. Thus, their number is by no means proportional to the number of cells in a spheroid; it rather controls the trade-off between the computational complexity and the accuracy of the simulation. For our simulations, we considered about 100 particles for each spheroid.

As mentioned in the methodology section, in the SPH method, the displacement of each particle is computed regarding its neighbouring particles. If we want to have only elastic objects, we need to compute each particle's neighbours only at the beginning of the simulation. However, in the case of plastic deformation, we need to update neighbours in each simulation iteration as the reference shape will differ in each time step. In the solid model, a volume conservation force does not allow spheroids to change their volume significantly. Therefore, we do not need to update each particle's neighbours as the reference shape is always the same.

For modelling the attraction force between spheroids, we utilized the Lennard-Jones potential force [52]. The Lennard-Jones potential is commonly employed to approximate the Van der Waals force between neutral atoms or molecules [53]. The following equation expresses the Lennard-Jones potential:

$$V(r) = 4\epsilon\left[\left(\frac{\sigma}{r}\right)^{12} - \left(\frac{\sigma}{r}\right)^{6}\right] \tag{9}$$

where $V(r)$ represents the potential energy between two particles at a distance r, ϵ denotes the depth of the potential well determining the strength of the interaction between particles, and σ is the distance at which the potential reaches its minimum value. Our observations indicate that spheroids only approach each other if sufficiently close (please refer to section ef sec:

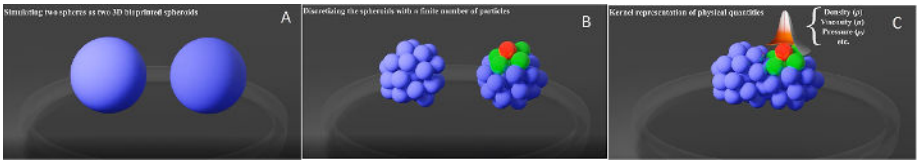

Figure 2. (A): Solid spheroids simulated. (B): Discretized spheroids using a finite number of particles (SPH uses neighbour particles—here the green spheres—to compute a physical quantity of the centre particle—here the red particle. (C): Kernel distribution (the shape distribution) over a particle's neighbours using the SPH method. The full video is available here.

validation). We can achieve such behaviour with the Lennard-Jones potential by tuning the parameters σ and ϵ. The potential becomes zero beyond a certain distance and increases as the distance between spheroids decreases. To convert this potential energy into an attraction force, we need to compute the derivative of the potential energy with respect to the particles' distance r.

Additionally, as explained in section 1, we establish connections between particles belonging to different spheroids when they get in contact. We used this approach to model surface adhesion force.

For implementing the SPH solid and fluid models, we have used a polynomial kernel to distribute mass around each particle:

$$W^{\text{poly}}(r,h) = \frac{315}{64\pi h^9}\begin{cases}\left(h^2-r^2\right)^3 & \text{if } 0 \leqslant r \leqslant h\\ 0 & \text{otherwise}\end{cases} \tag{10}$$

where r is the distance to the particle, and h is the kernel's support. There are a couple of properties that the smoothing kernel has to obey. First, the influence of particles at a distance of H from the selected particle must drop away to zero as H increases. This means that particles that are far away do not interact with selected particles. The second is that W has to sum to 1 over a sphere of radius H.

Therefore, the density at particle i can be obtained as:

$$\rho_i = \sum_j m_j w_{ij}, \tag{11}$$

where $w_{ij} = W(|x_j - x_i|, h_i)$ and the volume of the particle i is given by $v_i = m_i/\rho_i$. We have used an MLSs approximation of the displacement field to solve the differential equations related to deformation. Therefore, we can make an elastic-plastic system that is able to keep its shape by adding some internal force to each particle in case we have external compressive and tensile forces.

Hence, in each frame of the simulation, we need to solve a set of differential equations and update the internal force of each particle. We set the simulation time step and velocity damping to 0.01. The pseudo-code of the simulation loop is shown in algorithm 1.

In some simulations, we assumed elastic collisions between particles. In an SPH simulation, an elastic collision between two particles occurs when they collide and bounce off each other without any loss of kinetic energy [42]. In this case, particles are considered to have collided when the distance between them is less than the radius of one of the particles. Suppose particles i and j have collided. To update their velocities, we can use the following formula:

$$\begin{aligned} v_i &= v_i - \frac{2m_j}{m_i+m_j}\frac{< v_i - v_j, x_i - x_j >}{\|x_i - x_j\|^2}\\ v_j &= v_j - \frac{2m_i}{m_i+m_j}\frac{< v_j - v_i, x_j - x_i >}{\|x_j - x_i\|^2} \end{aligned} \tag{12}$$

where v_i and v_j are the velocities of particles i and j, respectively, and m_i and m_j are the masses of particles i and j, respectively. $<,>$ denotes the inner product operator [54].

Algorithm 1. Simulation loop of solid-based model

```
for all particle i do
    Internal force ← 0
    Acceleration ← 0
    Displacement ← New position − Rest position
end for
for all particle i do
    Compute ∇u
end for
for all particle i do
    Compute strain → ε
    Compute stress → σ
    Compute internal force → F_internal
end for
for particle i do
    for particle j do
        Compute elastic collision
        update particle i velocity
        update particle j velocity
    end for
end for
for all particle i do
    Update acceleration
    Update velocity
    Update position
end for
```

The simulation frame in the fluid-based model is similar to the solid-based model. However, we do not have a volume conservation force as we have plastic

deformation, and hence can not guarantee that spheroids will keep their volume during the merging process. Instead, we have added pressure and viscosity as new forces in the model. Also, we need to update each particle's neighbourhood in each simulation iteration as we may have plastic deformation and, consequently, a change in the reference shape. One of the simulation's major computational components is updating each particle's neighbours in each iteration. For determining each particle's search radius, H, we first obtained the 15 nearest neighbours for each particle. Then we set the neighbour's search radius as the maximum distance of each particle to its initial neighbours. Then, we keep this radius for the rest of the simulation and find each particle's neighbours based on the KDTree data structure.

In the fluid-based model, we aim to represent the dynamics of the spheroids by a set of particles. We will do that by taking the material derivative of the equation of motion. The material derivative is the derivative along a path with a given velocity. Hence, particles will be travelling along this path in space. The equation that we actually will solve for each particle i is:

$$\frac{\mathrm{d}v_i}{\mathrm{d}t} = g - \frac{1}{\rho_i}\nabla p + \frac{\mu}{\rho_i}\nabla^2 v \tag{13}$$

where μ is the viscosity, ρ is density and ∇p is the pressure gradient. In particular, we have simplified the incompressible Navier–Stokes equation by taking the material derivative so that we have a simple equation for the motion of one particle.

According to the Navier–Stokes equation, the density term of each particle can be approximated by its neighbours' masses using the SPH kernel function (see equation (11)). For the fluid-based model, we have used a polynomial kernel (equation (10)) for approximating density, just like the solid-based model. The above equation says that ρ, the density, is approximately equal to the sum of the masses of nearby points weighted by the smooth kernel W. Also, we approximate the pressure gradient as follows:

$$\frac{\nabla p_i}{\rho_i} \approx \sum_j m_j \left(\frac{p_i}{\rho_i^2} + \frac{p_j}{\rho_j^2}\right) \nabla W\left(r_i - r_j, h\right). \tag{14}$$

Here, W is, in fact, a vector expression, and because a gradient is an effector, as a result, this whole approximation has an effective value, which is what we would expect for the gradient of p. W is the Spiky kernel function, and it is defined as:

$$W^{\text{spiky}}(r,h) = \frac{15}{\pi h^6}\begin{cases}(h-r)^3 & \text{if } 0 \leqslant r \leqslant h\\ 0 & \text{otherwise}\end{cases} \tag{15}$$

where r is the distance to the particle, and h is the kernel's support. The reason for using this kernel instead of the polynomial kernel provided in equation (10) is that the spiky kernel generates repulsion forces near the centre of the kernel and avoids particles clustering around the centre of the kernel.

Finally, the last term that should be approximated is viscosity which can be computed as:

$$\frac{\mu}{\rho_i}\nabla^2 v_i \approx \frac{\mu}{\rho_i}\sum_j m_j \left(\frac{v_j - v_i}{\rho_j}\right) \nabla^2 W\left(r_i - r_j, h\right) \tag{16}$$

where μ is a scalar coefficient that defines the viscosity of the fluid. If μ has a small value, it is a relatively non-viscous fluid like water; if μ has a large value, it can be a relatively viscous fluid. v_i is the velocity of particle i and ρ_i is density of particle i. Also, for the viscosity force, we need to use a kernel whose Laplacian is positive everywhere. Thus we define W in equation (16) as:

$$W^{\text{viscosity}}(r,h) = \frac{15}{2\pi h^3}\begin{cases}-\frac{r^3}{2h^3} + \frac{r^2}{h^2} + \frac{h}{2r} - 1 & \text{if } 0 \leqslant r \leqslant h\\ 0 & \text{otherwise}\end{cases}. \tag{17}$$

Note that there is a vector subtraction in the equation (16); if two particles have the same velocity, the viscosity force will be zero. It means that there will be no viscous interaction between them. On the other hand, if the vectors are slightly different, they will have a small viscous interaction. They will have a relatively large viscous interaction if they differ significantly. Hence, we can see how this term encourages the particles to travel together or move in the same direction over time. In fact, particles near each other and travelling in the same direction will not influence each other. However, particles that are near each other and travelling at different velocities will influence each other and try to pull each other together into a common velocity. The simulation framework of the fluid-based model is explained in algorithm 2:

Algorithm 2. Simulation loop of fluid-based model

for all particle i
  $Pressure force \leftarrow 0$
  $Viscosity force \leftarrow 0$
  $Elastic-plastic force \leftarrow 0$
  $Acceleration \leftarrow 0$
  $Displacement \leftarrow New position - Rest position$
end for
for all particle i **do**
  Update neighbourhoods
end for
for all particle i **do**
  $Update density \rightarrow \rho$
  $Update pressure \rightarrow p$
  $Update volume \rightarrow v$
end for
for all particle i **do**
  $Compute pressure force \rightarrow f_{press}$
  $Compute viscosity force \rightarrow f_{viscos}$
end for
for all particle i **do**
  $Compute \nabla u$
end for
for all particle i **do**
  $Compute strain \rightarrow \varepsilon = \varepsilon^p + \varepsilon^e$
  $\varepsilon' = \varepsilon^e - \frac{Tr(\varepsilon^e)}{3}\mathbf{I}$
  $Compute stress\, \sigma$
  if $\gamma 1 \leqslant \|\varepsilon'\|$ **then**
    $\Delta\varepsilon^p = \frac{\|\varepsilon'\| - \gamma 1}{\|\varepsilon'\|}\varepsilon'$
    $\varepsilon^p = (\varepsilon^p + \Delta\varepsilon^p)\min(1, \frac{\gamma 2}{\|\varepsilon^p + \Delta\varepsilon^p\|})$
  end if
  $Compute elastic-plastic force \rightarrow \mathbf{f_{ep}}$
end for
for all particle i **do**
  $F_{Total} = f_{press} + f_{viscos} + f_{ep}$
  $Update acceleration$
  $Update velocity$
  $Update position$
end for

In the next section, we will show samples of our simulation results with their corresponding parameters and compare them with actual experiments to see how much our models can describe the spheroids' mechanical behaviour during the merging process.

2.4. Surface reconstruction

The physical simulation updates the position of the particles at every loop. We use the list of particle positions for each frame to produce a temporal sequence of 3D triangle meshes representing the spheroid fusion process. The surface reconstruction program is written in C++ and based on the OpenVDB library [55] for sparse volumetric processing. The created meshes can then be exported as OBJ files or visualized with the interactive viewer included in our program.

We operate on implicit surfaces in the form of narrow-band level sets, in order to avoid dealing with topological changes of the surface, such as merging events. We use the implementation of narrow-band level sets provided by OpenVDB. Initially, the first frame of the simulation sequence is used to generate an implicit representation of the spheroids. In order to do so, we first determine the spheroid to which each particle belongs, with a simple clustering step. Then, assuming that the spheroids are perfect spheres in their initial state, we create the starting implicit surface. Finally, we create the initial mesh with OpenVDB's isosurface extraction utility, which is conceptually similar to the dual marching cubes algorithm [56].

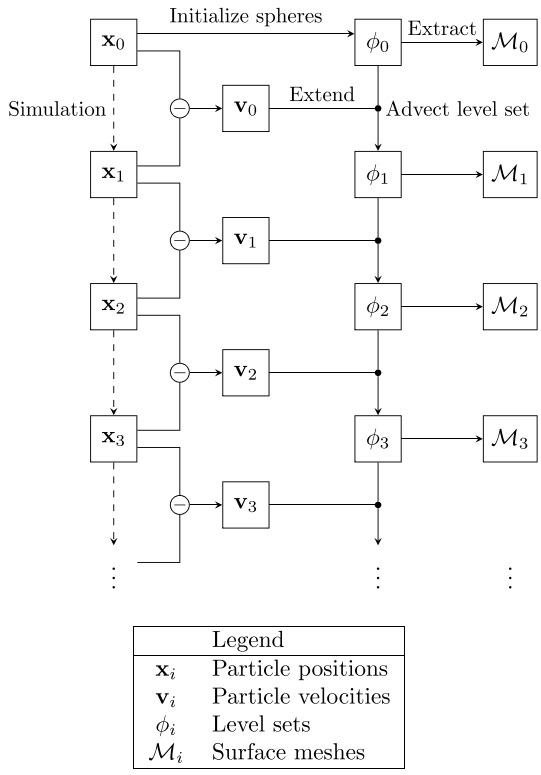

Figure 3. Diagram of the surface reconstruction algorithm.

For every frame, except the last, we determine the velocity of each particle by the difference with the next frame in the sequence (figure 3). We treat this information as a sparse sampling of a globally-defined velocity field, which we reconstruct with kernel interpolation. The global velocity field is then used to deform and displace the implicit surface, via level set advection, to produce the next implicit surface. By construction, the advected surface follows the motion of the particle system. We make use of OpenVDB's advection solver for this purpose. The generated implicit surface serves as the starting point for the next advection step, and it is also used to produce the corresponding frame's mesh, again via isosurface extraction.

The reconstruction process has several parameters that can be tuned to manage the trade-off between surface quality and execution times. These include grid coarseness for the implicit surfaces, the width of the narrow band, and meshing adaptivity.

Table 1. Simulation parameters and their change steps.

Parameter (abbreviation)	Range	Change step
Young modulus (YM)	0.5–3.5	0.5
Poisson ratio (PR)	0.35–0.49	0.04
Volume constant (VolC)	0.1–2	0.5
Plastic limit (PL)	0–0.9	0.1
Stiffness (S)	0.1–3	0.5
Rest density (RD)	0.1–2.5	0.4
Viscosity coefficient (VC)	0.1–3	0.5

3. Results

In this section, we provide the results of our simulations with different parameters. All code is implemented in Python and C++ programming languages. For computation, we have used a notebook with AMD Ryzen PRO 4750U and Radeon Graphics 1.70 GHz. OpenGL platform and OpenVDB [57] have been utilized for visualization and surface extraction. Also, the results were rendered with the Blender software.

We defined a range of changes for each parameter to see the effect of that parameter on the simulation result. For this purpose, we have summarized the range of each parameter we have used in our simulation in table 1.

In our experiments, stiffness, rest density and viscosity coefficient are only used in the fluid model, and the rest of the parameters are common between the fluid and the solid-based models.

As mentioned in the implementation section, we performed 46 simulations with different combinations of the parameters in table 1 to simulate different behaviour of spheroids during the merging process. The primary purpose of this series of simulations is to show the flexibility of the proposed physically-based framework in matching the different parameters involved in the spheroid merging process. In the following subsections, we show just some selected results. Also, the developed framework is generic so that it is able to be used for simulating different applications with the same material properties or with more than two spheroids (figure 4).

3.1. Simulations without surface

The first set of results only contains particles (without surface reconstruction) to show how the simulation is working. The simulation parameters and the full video link of each simulation are provided in the caption of the figures. Based on the video, spheroids first go toward each other and then start bouncing back and expanding a little bit due to the elastic force. (figures 5 and 6).

3.2. Simulations with surface

In the next set of results, we will show the fusion process of spheroids with their surfaces. This set of results can mimic the actual process using appropriate parameters. Therefore, we will present at least one example of each model (solid or fluid) with different simulation parameters.

In figure 7, selected frames of a solid-based simulation are shown. In this set of results, the spheroid surfaces have been extracted and shown with different colours (red and green). As expected, the surface's behaviour depends on moving particles connected to the surface.

Based on our surface extraction algorithm, surfaces start joining at the beginning of the simulation to form a final shape of the fused spheroids. However, we can see different kinds of deformation on the surface during the simulation caused by the interior interaction of the spheroid particles.

Figure 8 shows two selected simulations of solid-based models. The main differences between these two simulations are plastic limit and Poisson ratio parameters which are 0.1 and 0.45 for figure 8(a), and 0.9 and 0.35 for figure 8(b), respectively. The effects of these parameters are clearly seen, as the volume of spheroids in figure 8(a) has decreased a lot due to having more plastic properties. Hence, we can see in figure 8(a), there is more plastic deformation in the spheroids.

Based on the theory of continuum mechanics, decreasing Young's modulus or increasing the Poisson ratio will make a more elastic object. To prove this fact, in figure 9, we compared four simulations in which we decreased Young's modulus and increased Poisson ratio from top left to bottom right, respectively. It can be seen that with decreasing Young modulus and increasing Poisson ratio, the volume and area of spheroids change significantly.

It is worth mentioning that gravitational force is applied to each spheroid particle toward the other spheroid's centre. As a result, due to the spheroids' visco-elastic properties, this gravitational force causes the spheres to crumple and lose volume during the fusion process. However, surprisingly, we see an increase in volume and area in the last simulation. This can be due to the dominance of the elastic force, which tends to return the spheroid to the initial shape, over the gravity force, which tends to crumple the spheroids. Because in the last simulation, Poisson's coefficient and Young's modulus have their maximum value, and the spheres have assumed the most elastic state (figure 9).

The results of simulating as visco-elastic fluids for full (figure 10(a)) and partial (figure 10(b)) fusion are shown in figure 10. The meaning of partial or full fusion is the degree of interpenetration of the spheroids, which can be adjusted by varying the attraction force between them and an opposing external force caused by the hydrogel. The parameter values of each simulation can be seen in the caption of the figures. In this result, spheroids have an egg-shaped deformation in complete fusion. This is because of

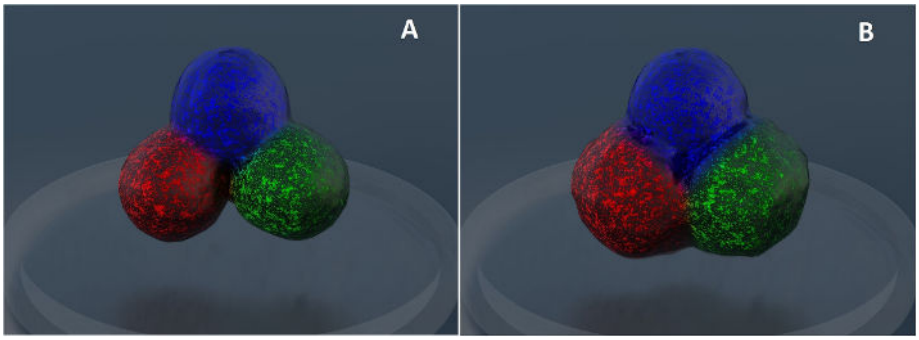

Figure 4. Simulation of fusion of three spheroids: (a) frame 1 of the simulation (beginning of the fusion), (b) frame 100 of the simulation (middle of the fusion).

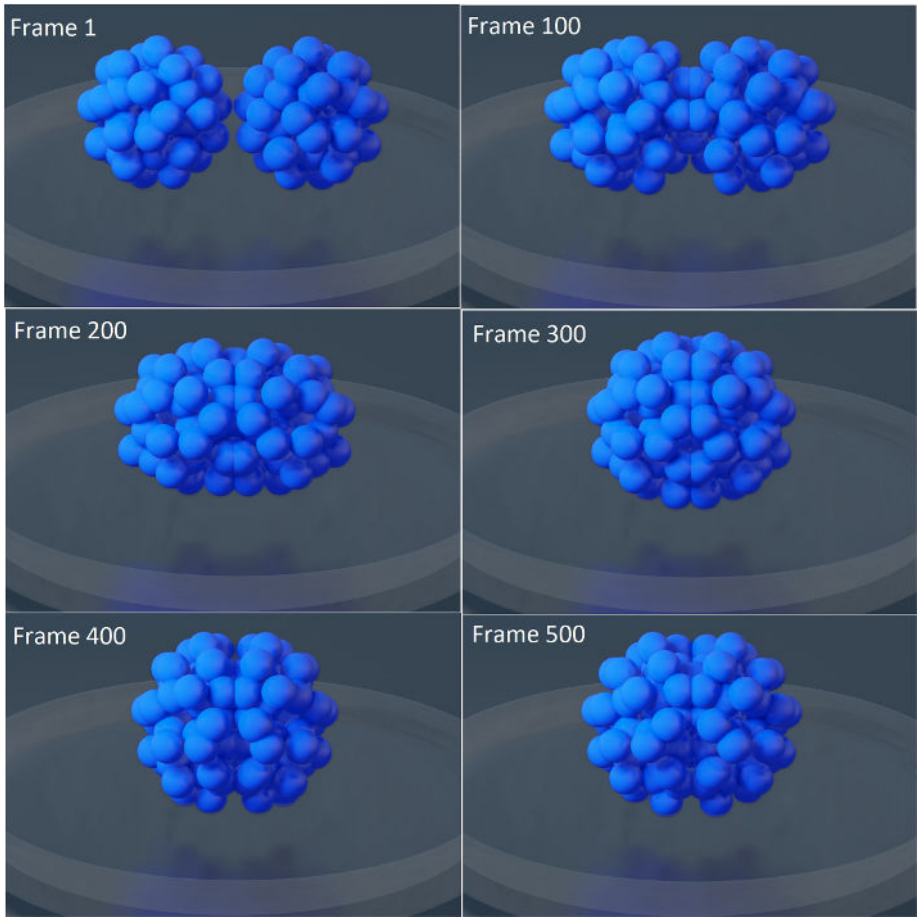

Figure 5. Fusion process of spheroids in 500 simulated frames using the fluid-based SPH model and without surface reconstruction (parameters: YM = 3, PR = 0.4, VolC = 1.4, PL = 0.1, S = 1, RD = 1, VC = 1). The full video is available here.

the continual gravitational force between spheroids particles, which forces the particles to spread along the edge of spheroids collision. The other important difference between figures 10(a) and (b) is the stiffness parameter which is 0.5 for figure 10(a) and 1 for 10(b) That is why we can see a little shrinkage in spheroid volume in figure 10(a).

To better understand the effect of stiffness and constant volume parameters, figure 11 shows the last frame four simulations in which we have an increase in volume constant and stiffness parameters from bottom left to top right. As it might be hard to see the amount of deformation in the total configuration due to the size of the images, we have measured the area and volume of the total configuration at the beginning and end of each simulation. Of course, at the beginning of all simulations, the area and volume of the configuration are fixed and equal to $3.88 \times 10^{13} \mu m^2$ and $1.66 \times 10^{19} \mu m^3$, respectively. Increasing either volume constant or stiffness will increase the volume and area of the total spheroid configuration except for the last picture (top right of

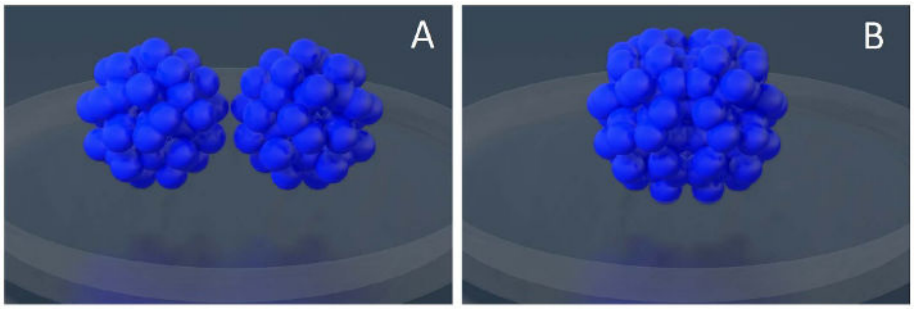

Figure 6. A: The beginning of the simulation when spheroids move towards each other. B: The end of the simulation when particles are stabilized (parameters: YM = 3, PR = 0.45, VolC = 1.4, Pl = 0.3, S = 1, RD = 1.5, VC = 1). The full video is available here.

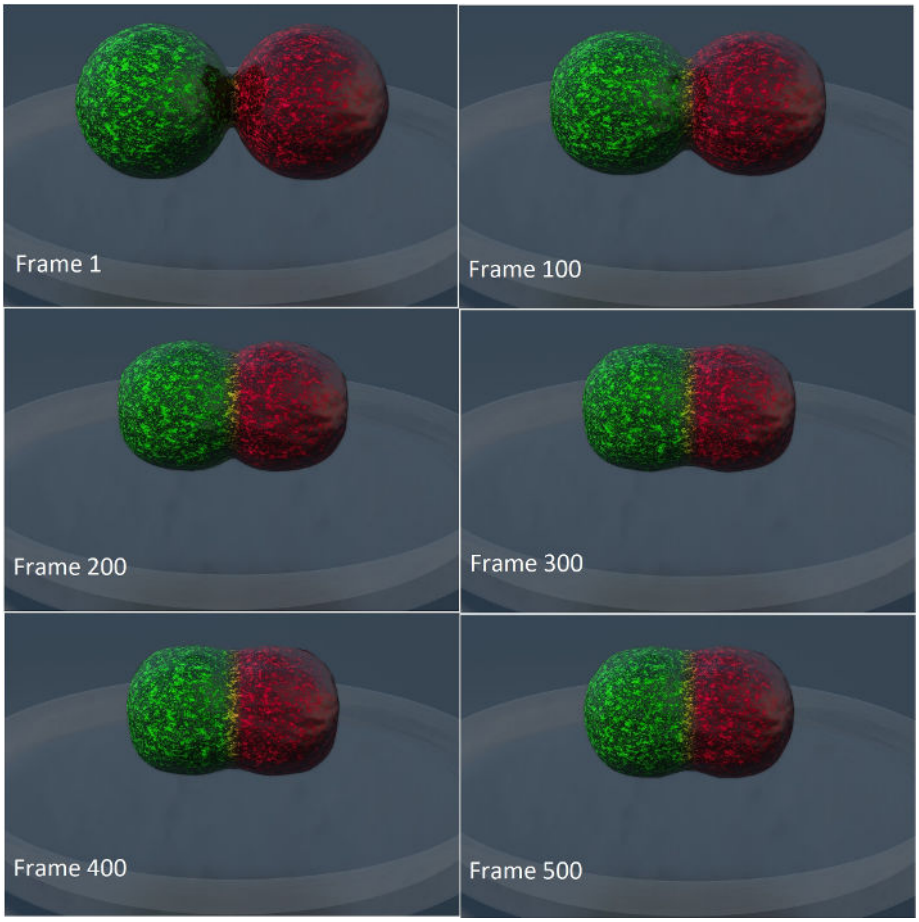

Figure 7. Fusion process of spheroids in 500 simulated frames using the solid-based SPH model with surface extraction (parameters: YM = 1, PR = 0.45, VolC = 1.4, PL = 0.1). The full video is available here.

figure 11). This exception is due to the balancing of the forces and stability in the position of the particles. The volume constant, stiffness, area and volume of each simulation are written at the bottom or above each picture.

Another kind of simulation is when we applied elastic collision between particles of two spheroids. In this case, when two spheroids touch each other, their particles collide and bounce back due to the elastic collision force. Then, the attraction force brings them back together, and they collide again. This process will repeat until the particles get balanced in a final position. As shown in figure 12, when we have elastic collision in our simulation, spheroids do not get entirely merged as particles of each spheroid do not go through each other. Indeed, particles get spread along the boundary of collision.

In the simulations of figure 12, we have used two different plastic limit values. It is evident that the simulation with a larger plastic limit shows more plastic deformation (figure 12(b)).

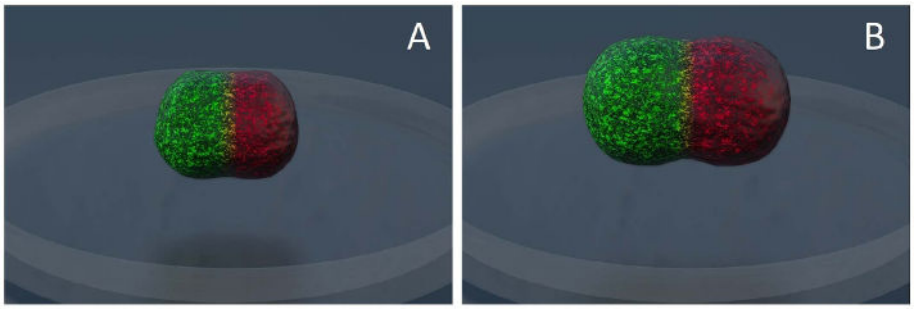

Figure 8. (A): Complete fusion of spheroids made by the visco-elastic solid model (parameters: YM = 3, PR = 0.45, VolC = 1.4, PL = 0.9). The full video is available here. (B): Half fusion of spheroids made by the visco-elastic solid model (parameters: YM = 3, PR = 0.35, VolC = 1.4, PL = 0.1). The full video is available here.

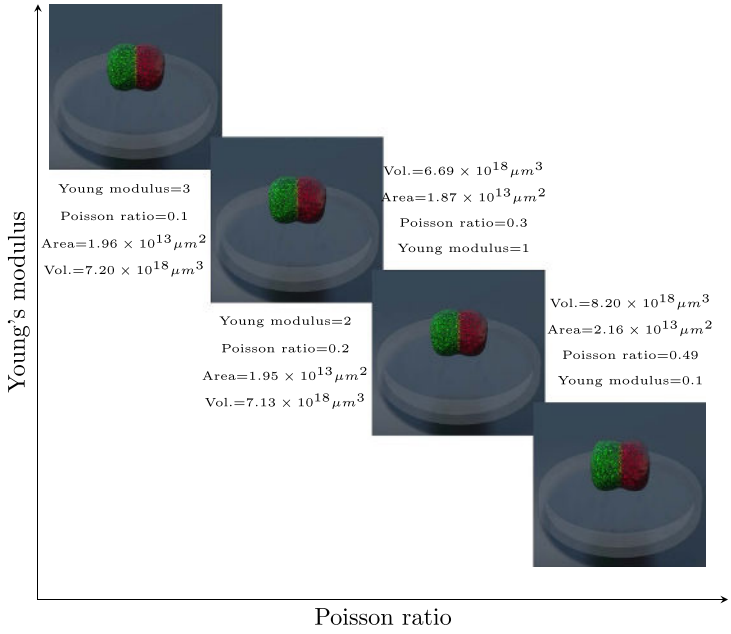

Figure 9. Effect of increasing Poisson ratio and Young's modulus on total area and volume (total deformation) of spheroids.

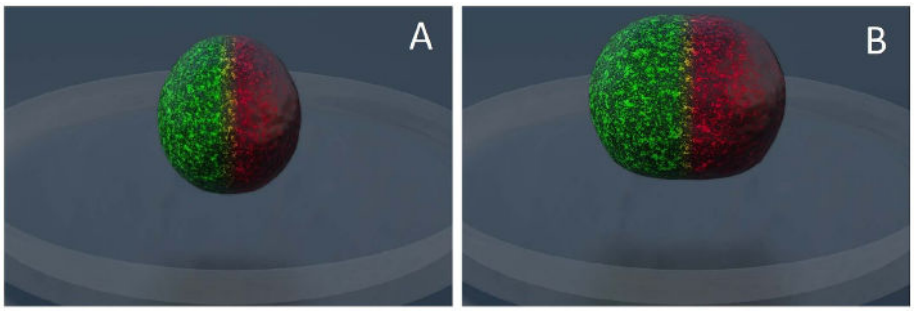

Figure 10. (A): Complete fusion of spheroids made by the visco-elastic fluid model (parameters: YM = 3, PR = 0.45, VolC = 1.4, PL = 0.1, S = 0.5, RD = 1, VC = 1). The full video is available here. (B): Half fusion of spheroids made by the visco-elastic fluid model. (parameters: YM = 3, PR = 0.45, VolC = 1.4, PL = 0.1, S = 1, RD = 1, VC = 0.5). The full video is available here.

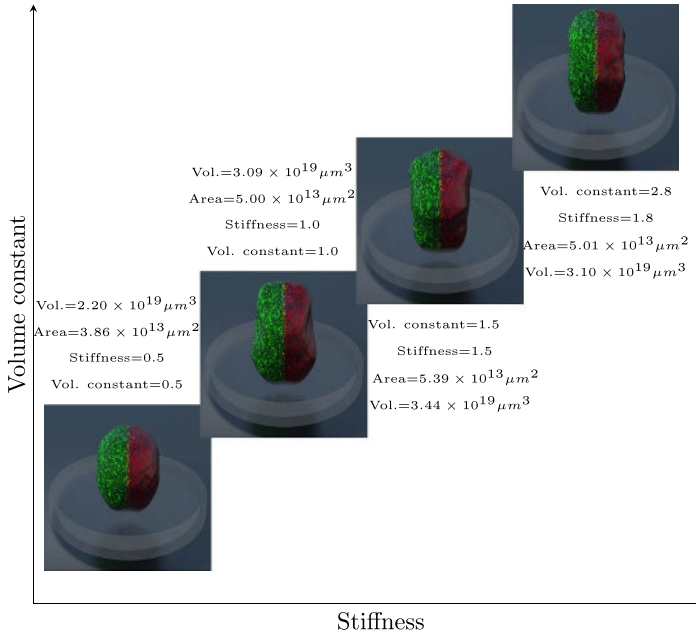

Figure 11. Effect of increasing stiffness and volume constant on spheroids total area and volume (total deformation).

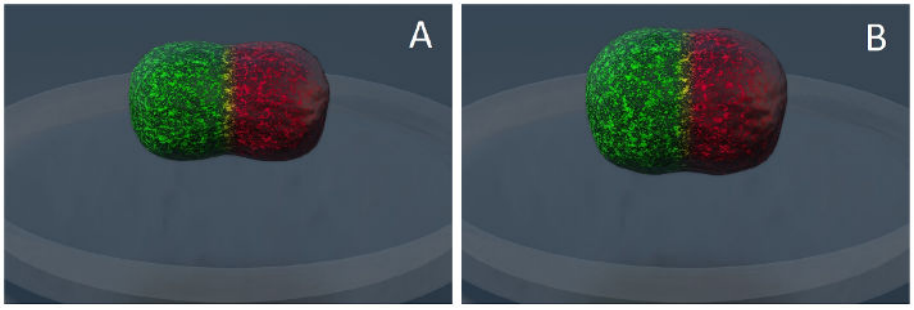

Figure 12. (A): Merging of spheroids made by the visco-elastic solid model with less plastic deformation (YM = 0.5, PR = 0.45, VolC = 1.4, PL = 0.1). The full video is available here. (B): Merging of spheroids made by the visco-elastic solid model with more plastic deformation (YM = 3, PR = 0.45, VolC = 2, PL = 0.5). The full video is available here.

4. *In-vitro* validation

In order to validate the effectiveness of the presented mathematical models, we have conducted a series of practical experiments to compare the results obtained from the simulation with images obtained from the actual fusion of spheroids. We designed our experiments based on potential factors that might affect the fusion process namely: the Hydrogel type, the density of spheroids, and the distance between spheroids. In this section, we present our experiments and discuss the validation results.

4.1. Design of experiment

We have considered 36 different scenarios corresponding to four types of hydrogel, three different densities of spheroids and three different distances between spheroids. We conducted a full factorial experiment with three replications for each combination of parameters leading to a total of 108 experiments *in vitro*.

First, three types of cells were cultured:

- Human Cardiac Fibroblasts Cells (HCFCs)
- Human Coronary Artery Endothelial Cells (HCAECs)
- Human Cardiac Myocytes Cells (HCMCs)

Each type of cell was grown using its specific media and growth protocol. After growing a sufficient number of cells, we made spheroids by combining them. A 384-hanging drop culture plate was used to culture cells in it. Based on previous studies, the three types of cells, HCFCs, HEAECs and HCMSs, are combined with a ratio of 1:1:2 to form spheroids. The culture plate is incubated at 37 degrees (average

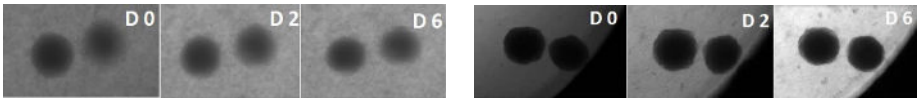

(a) (b)

Figure 13. An example of two spheroids that are relatively close but are not fused within six days: (a) Environment: hydrogel 1, density: 20 000 cells, distance: close, (b) Environment: hydrogel 2, density: 30 000 cells, distance: close.

human body temperature) for 4 to 5 days to generate human spheroids. Cardiac spheroids usually have a diameter of around 100–200 μm and volume of around $4.2 \times 10^6 - 3.4 \times 10^7 \mu m^3$. For more details on this process, please refer to Polonchuk *et al* [18].

Hydrogel

The stiffness of the hydrogel in which the spheroids get printed is usually the most critical factor, because its stiffness may prevent the spheroids from approaching each other. In order to produce different types of fusion, we have prepared four types of hydrogel based on their stiffness:

- Hydrogel 1: alginate/gelatin
- Hydrogel 2: alginate/gelatin+1% silk
- Hydrogel 3: alginate/gelatin+2% silk
- Hydrogel 4: alginate/gelatin+3% silk

Adding more silk will make a stiffer hydrogel and make spheroid movement harder.

Density of the spheroids

We measured the number of combined cells per spheroid while forming the spheroids. In this way, we can obtain different spheroids densities. For this study, we considered three different spheroids densities:

- spheroids with 10 000 cells
- spheroids with 20 000 cells
- spheroids with 30 000 cells

Distance of the spheroids

We considered three different distances between pairs of spheroids:

- very close distance ($dist. \leqslant 400\ \mu m$)
- close distance ($400\ \mu m \leqslant dist. \leqslant 700\ \mu m$)
- far distance ($dist. \geqslant 700\ \mu m$)

4.2. Results of validation

After placing spheroids in a well-plate, we monitor their fusion within six days by taking an image at different times. Our observations show that spheroids behave differently depending on the distance and the environment they are in. A detailed investigation of this hypothesis requires statistical tests that it is beyond the scope of this article. However, examination of the images shows that some spheroids do not fuse at all, some have little fusion, some have moderate fusion, and some are entirely fused. Most complete fusions occur in hydrogel 1 (alginate/gelatin), which is less stiff than other hydrogels. In contrast, spheroids fusion can be seen among all densities of spheroids. In terms of the distance between spheroids, all fusion occurred among the spheroids with very close distances. Hence, it is obvious that the distance is a very significant factor in our experiments and all fusion results presented in sections 4.4–4.6 are belonged to the 'very close distance' category.

4.3. No fusion

Some of the spheroids in the experiments did not fuse at all. The reason can be the time, hydrogel and distance. Most fusions happen within the first few minutes of the spheroids being close to each other. Since placing the spheroids in a well plate is a relatively time-consuming process, it may prevent their fusion during the experiment. Because according to our observation, fused spheroids start their fusion at the very beginning of being beside each other, and if they are not close enough, the chance of fusion decreases as time elapses. Stiffer hydrogel makes the fusion harder—as the second factor that affects the fusion process. The last factor is distance. Our observations show that all fusions have happened with spheroids that are very close to each other. Apparently, the gravitational force between them is weaker than the viscosity force of the hydrogel. Below it can be seen two examples of non-fusion of spheres over six days (figure 13).

4.4. Low Fusion

Another case of fusion is when there is little fusion between the spheroids. Based on our observations, this mode is the most common among the fusion types, especially when spheroids are embedded in a hydrogel (figures 14 and 15). The proposed simulation framework can successfully simulate this type of fusion in different cases. Table 2 compares experiment and simulation parameters of figures 14 and 15.

4.5. Medium fusion

In some cases, the spheroids fuse to a greater extent, which we call moderate fusion. Examples of this type of fusion are presented below (figures 16 and 17). This type of fusion can be simulated via the proposed

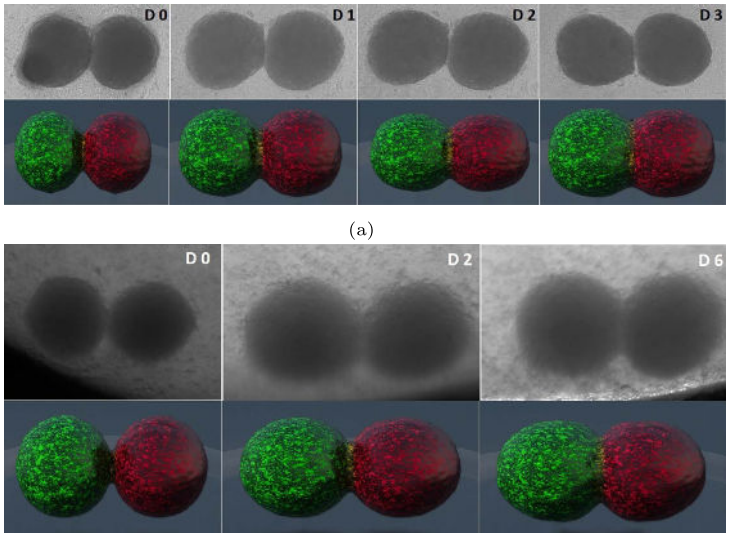

Figure 14. Two examples of a pair of spheroids that have low fusion: (a) environment: hydrogel 1, density: 10 000 cells, (b) environment: hydrogel 1, density: 10 000 cells, (c) environment: hydrogel 2, density: 20 000 cells.

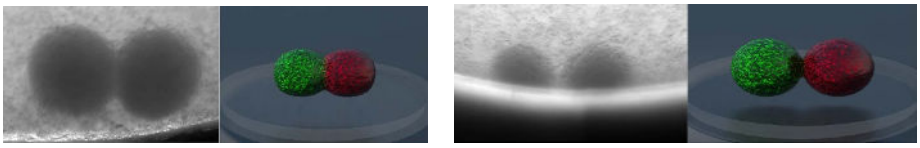

Figure 15. Two examples of two spheroids that have low fusion at the sixth day: (a) Environment: hydrogel 2, density: 20 000 cells, (b) Environment: hydrogel 3, density: 20 000 cells.

Table 2. Comparing experiment parameters and simulation parameters for low fusion.

Figure	Experiment parameters	Simulation parameters
figure 14(a)	Environment: hydrogel 1 Density: 10 000 cells	Young modulus: 3 Poisson ratio: 0.35 Volume constant: 1.4 plastic limit: 0.1
figure 14(b)	Environment: hydrogel 1 Density: 30 000 cells	Young modulus: 2.6 Poisson ratio: 0.38 Volume constant: 1.5 plastic limit: 0.2
figure 15(a)	Environment: hydrogel 2 Density: 20 000 cells	Young modulus: 3 Poisson ratio: 0.3 Volume constant: 1.5 plastic limit: 0.2
figure 15(b)	Environment: hydrogel 3 Density: 20 000 cells	Young modulus: 2.5 Poisson ratio: 0.3 Volume constant: 1.5 plastic limit: 0.2

models appropriately. Table 3 compares experiment and simulation parameters of figures 16 and 17.

4.6. Complete fusion

The last case is the complete fusion of the spheroids, in which they merge almost completely and usually form a larger spheroid. Below are examples of the complete fusion of spheroids and their corresponding simulations. This type of fusion usually has the largest deformation in the final shape of the fused spheroids. As it is shown in figures 18 and 19, our simulator has the ability to simulate the

Table 3. Comparing experiment parameters and simulation parameters for medium fusion.

Figure	Experiment parameters	Simulation parameters
figure 16	Environment: hydrogel 1 Density: 10 000 cells	Young modulus: 3 Poisson ratio: 0.35 Volume constant: 1.4 plastic limit: 0.1
figure 17(a)	Environment: hydrogel 4 Density: 20 000 cells	Young modulus: 2 Poisson ratio: 0.45 Volume constant: 1.5 plastic limit: 0.2 stiffness: 1 rest density: 1 viscosity coefficient: 0.5
figure 17(b)	Environment: hydrogel 1 Density: 30 000 cells	Young modulus: 2.8 Poisson ratio: 0.35 Volume constant: 1.5 plastic limit: 0.6

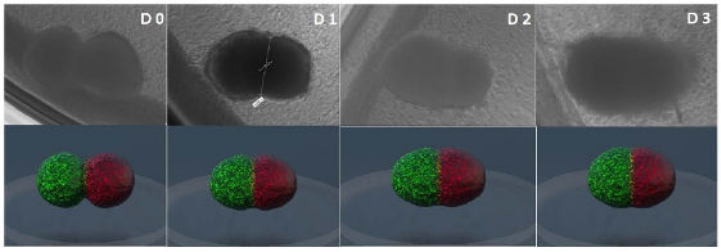

Figure 16. An example of two spheroids that have medium fusion within three days: Environment: hydrogel 1, density: 10 000 cells.

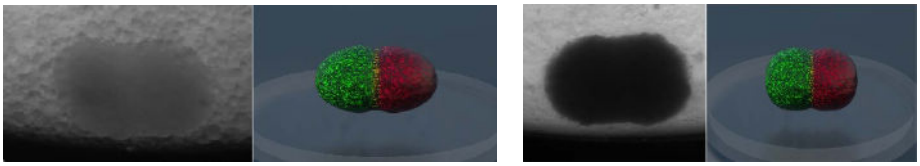

(a) (b)

Figure 17. Two examples of two spheroids that have medium fusion at the sixth day: Environment: (a) hydrogel 4, density: 20 000 cells, (b) Environment: hydrogel 1, density: 30 000 cells.

corresponding deformation in the spheroids. Table 3 compares experiment and simulation parameters of figures 18 and 19.

This section's pictures show that the proposed models can simulate all fusion states between spheroids. Tables 2–4 compare biological and simulation parameters for the spheroids fusion. As we expected, for lower fusion, there is not much deformation on spheroids. Because of that, the physical parameters of the corresponding simulation are tuned to make a less deformable object (e.g. relatively larger Young modulus and less Poisson ratio). However, the more fusion the spheroids have, the more deformation they will have. Hence, the physical parameters of the corresponding simulation for higher fusion are tuned to make a softer object.

Since all fusions occur only when the distance between spheroids is very close ($\leqslant 400\mu$m), therefore, the distance in all the simulations is supposed to be very close (in the scale of the simulation).

4.7. Morphological analysis

Morphology plays a crucial role in spheroid fusion, as it characterizes the geometric properties of the spheroids throughout the fusion process. To validate our model and simulations, it is essential to compare the morphological aspects between *in-silico* simulations and *in-vitro* experimental data.

Following the methodology introduced by Susienka *et al* [58], we defined three variables–length, width, and the length of the contact area of spheroid doublets–to represent the spheroid morphology

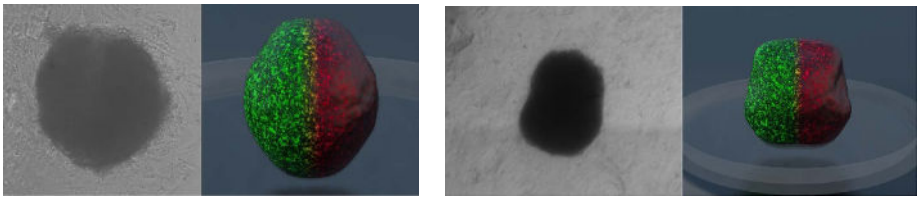

(a) (b)

Figure 18. Two examples of two spheroids that have complete fusion at the sixth day: (a) Environment: hydrogel 1, density: 10 000 cells, (b) Environment: hydrogel 1, density: 20 000 cells.

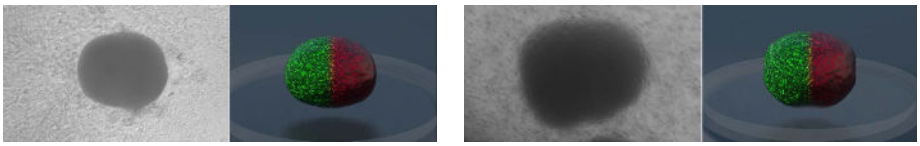

(a) (b)

Figure 19. two example of two spheroids that have complete fusion at the sixth day: (a) Environment: hydrogel 1, density: 10 000 cells, (b) Environment: hydrogel 2, density: 30 000.

Table 4. Comparing experiment parameters and simulation parameters for complete fusion.

Figure	Experiment parameters	Simulation parameters
figure 18(a)	Environment: hydrogel 1 Density: 10 000 cells	Young modulus: 0.5 Poisson ratio: 0.45 Volume constant: 1.5 plastic limit: 0.1 stiffness: 1 rest density: 1 viscosity coefficient: 1
figure 18(b)	Environment: hydrogel 1 Density: 20 000 cells	Young modulus: 0.8 Poisson ratio: 0.4 Volume constant: 1 plastic limit: 0.2 stiffness: 1 rest density: 0.8 viscosity coefficient: 0.5
figure 19(a)	Environment: hydrogel 1 Density: 10 000 cells	Young modulus: 1 Poisson ratio: 0.4 Volume constant: 1.5 plastic limit: 0.2
figure 19(b)	Environment: hydrogel 2 Density: 30 000 cells	Young modulus: 1.5 Poisson ratio: 0.4 Volume constant: 1.5 plastic limit: 0.3

during fusion (refer to figure 20). These variables were measured using Fiji software in the experimental data [59]. Similarly, the same variables were measured in the simulation data corresponding to the experimental conditions. The data were categorized into three fusion types: low, medium, and complete fusion. Subsequently, statistical tests were conducted to analyse the results, employing the t-test to compare the means of each variable between the *in-vitro* and *in-silico* datasets. The summary of the test results is presented in table 5.

The obtained p-values from the performed tests, as shown in table 5, indicate their relatively high values, rendering them statistically insignificant. This suggests that there is no significant difference between the mean values of each morphological variable in the experimental data and the simulations. Thus, the simulations successfully capture the observed morphological behaviour in the experiments.

For a more comprehensive analysis, figure 21 presents box plots illustrating the distribution of each variable for different fusion types in both *in-vitro* and

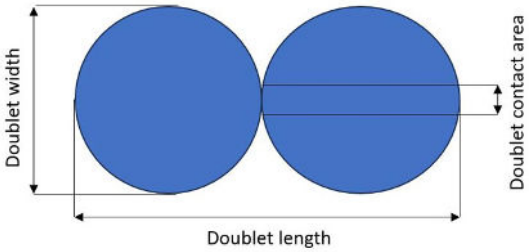

Figure 20. Morphological parameters measured during fusion.

Table 5. The results of t-test for comparing the mean of morphological variables for *in-vitro* and *in-silico* data.

Type of fusion	Morphological variables	Hypothesis	*p*-value
Low fusion	Doublet length	$H_0 : \mu_{in-vitro} = \mu_{in-silico}$	0.8333 (ns)[a]
	Doublet width		0.5277 (ns)
	Doublet contact area		0.9797 (ns)
Medium fusion	Doublet length	$H_0 : \mu_{in-vitro} = \mu_{in-silico}$	0.7997 (ns)
	Doublet width		0.3978 (ns)
	Doublet contact area		0.4062 (ns)
Complete fusion	Doublet length	$H_0 : \mu_{in-vitro} = \mu_{in-silico}$	0.8510 (ns)
	Doublet width		0.7885 (ns)
	Doublet contact area		0.1072 (ns)

[a] not significant

in-silico settings. These plots reveal a remarkable similarity in the distribution of variables between the *in-vitro* and *in-silico* data. Although the variance of the *in-vitro* observations is generally higher, as expected, these graphs effectively demonstrate the close resemblance between the experimental and simulated data in terms of mean and variance.

This morphological analysis provides compelling evidence that our simulations accurately reproduce the observed behaviour of spheroid fusion. By quantifying parameters such as contact area and doublet dimensions, we aimed to demonstrate the model's ability to describe the temporal evolution of tissue shape changes.

5. Discussion

Physically-based simulations, especially the SPH method, are highly sensitive to model parameters such as kernel radius and the number of neighbours for each particle. Therefore, to avoid any simulation breakdown, we fixed the simulation time step at 0.01 and set the search radius for each particle so that at the beginning of the simulation, each particle has 15 neighbours. Of course, after running the simulation, the number of neighbours for each particle may change.

In this section, we will discuss the sensitivity of the simulations to the various parameters of the developed models. Observing the performed simulations, some of which were displayed in the previous section, shows that Young's modulus, Poisson ratio, volume constant, and stiffness are the most influential parameters in controlling deformation in spheroids. After that, the plastic limit has the most significant effect in controlling the amount of deformation.

In the video of figure 5, when two spheroids move towards each other, they also expand their volume due to internal pressure. The model's volume constant and stiffness parameters can tune this internal pressure. Increasing the stiffness and volume constant parameters leads to an increase in volume.

The effect of internal pressure is also visible in figure 6, where after spheroids reach each other, each particle goes toward the other spheroids' particles and continues its movement until the particles get balanced in a final position. It means that particles move until the total force applied to them becomes zero. In the case of figure 5, the particles spread apart slightly due to the elastic force between particles. However, in the simulation of figure 6, we do not see any increase in volume in spheroids due to not increasing the stiffness parameter. Therefore, spheroids approach each other and get compressed slightly at the beginning, increasing density; consequently, internal pressure force spreads them out again.

It is worth mentioning that elastic-plastic parameters are considered in all simulations. However, we have only mentioned the most important parameters that cause the specific behaviour of the spheroids during the simulation. For example, in the case of figure 6, the most important parameters were stiffness and density.

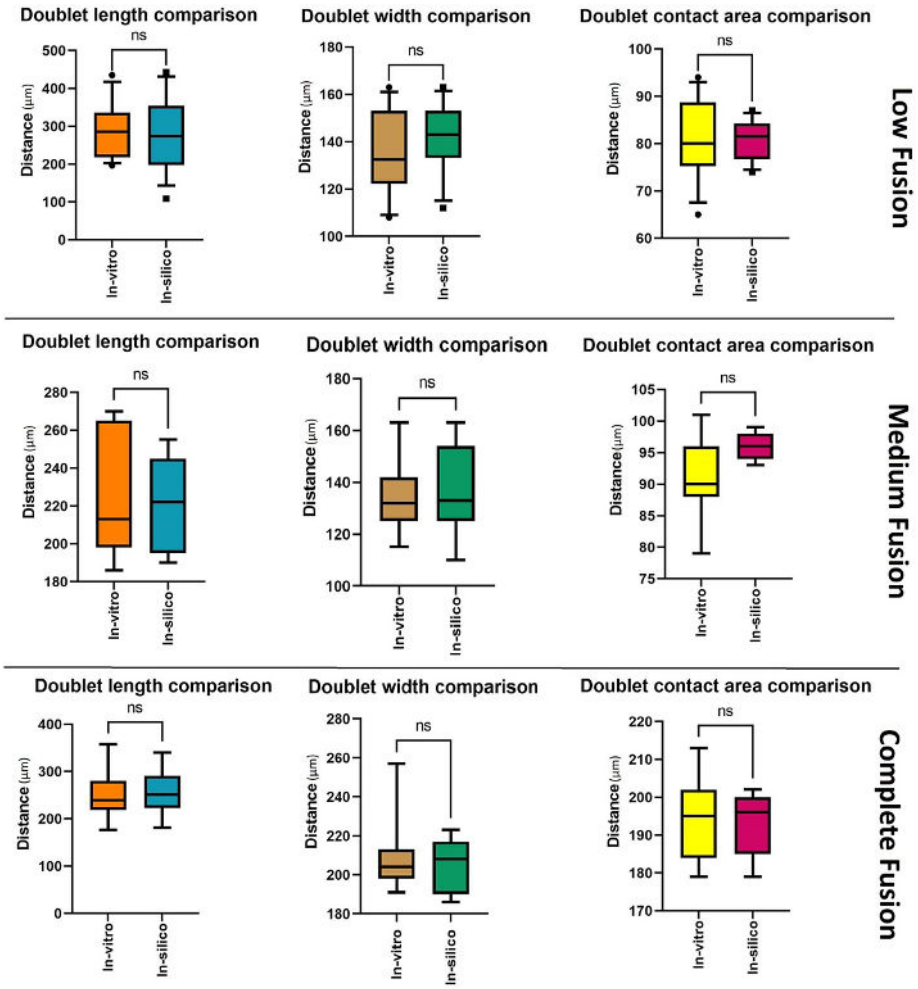

Figure 21. Box plots of morphological variables: the first row corresponds to the doublets length, width and contact area of low fusion, the second row corresponds to the doublets length, width and contact area of medium fusion, and the third row corresponds to the doublets length, width and contact area of complete fusion.

While the volume constant and stiffness are the most influential parameters in the fluid-based model, our observations show that Young's modulus and Poisson's ratio are the most critical parameters in the solid-based model. In figure 11, we compared four simulations while increasing their stiffness and volume constant to demonstrate the importance of these parameters. The results show that an increase in stiffness and volume constant will cause significant deformation in spheroids.

On the other hand, the effect of Young's modulus and Poisson's ratio is shown in figure 9, where we compared four simulations with different values of these parameters in terms of their total volumes and areas. The results indicate that increasing the Poisson's ratio and decreasing Young's modulus will cause more deformation in spheroids.

According to figure 9, from the top left to the bottom right of the graph, we have decreased the Poisson ratio and increased Young's modulus while we measured the final configuration's area and volume. All information about these simulations is mentioned at the bottom and above each picture. The interesting point of these simulation results is that by increasing the Poisson ratio and decreasing Young's modulus, we can see a decrease in volume and area except in the last simulation (bottom right of figure 9). We can conclude that increasing Poisson ratio and decreasing Young's modulus will give the spheroids more elastic properties. Therefore, we can be assured that our mathematical model and its implementation are valid. The exception that happened in the last simulation (bottom right of figure 9) is due to having the maximum Poisson ratio (0.49) and minimum Young modulus (0.1), which caused the spheroid to relax and increase the volume a little bit.

A final observation we would like to make about figures 9 and 11 is that simulated spheroids have a larger scale due to the ease of implementation compared to natural spheres. However, this difference does not affect the obtained results because the amount of deformation is scaled to the proportion of the initial and final shape of spheroids.

Another behaviour we aim to simulate is the external force caused by the interaction of the hydrogel and the spheroids. Although modelling the

interaction between these two forces is not one of the goals of this study, it can be considered a topic for future research. However, we considered this interaction the total external force applied to the spheroid particles. In that case, we should be able to simulate a half or complete fusion. This can be seen in the simulations of figures 8(a) and (b) where we consider the spheroids an elastic-plastic solid material.

As shown in figures 8 and 10, both solid and fluid simulation behaviours are very similar as elastic-plastic material is a phase between pure solid and pure fluids. The only difference between the two models is that spheroids change their volume permanently during the fusion process in fluid-based simulations. This is not the case in the solid model because the volume conservation force will suppress volume change in the spheroids. Therefore, the fluid model does a better job from this point of view, as in actual images, final merged spheroids are increased in volume.

To summarize the effect of the parameters on the model, we observed that a lower Young's modulus and larger Poisson ratio produce larger elastic properties in spheroids. Increasing the volume constant will increase the volume of spheroids (in case we do not have a volume conservation force). The elastic limit will tell us when the spheroids will switch to plastic deformation. Having a larger plastic limit allows spheroids to have more plastic deformation. Regarding fluid-specific parameters, stiffness affects the internal pressure of spheroids. The larger the stiffness, the larger the internal pressure and the increase in volume during the fusion. The simulation does not show significant sensitivity to the rest density parameter. Last but not least, increasing the viscosity coefficient will decrease the velocity of spheroids during the fusion.

5.1. Comparison with previous studies

Our study introduces a novel approach for simulating bioprinted spheroid fusion, making it the first framework in the literature to combine graphical simulation and SPH for bioprinting simulation. While Göhl and colleagues [27] also present a computer-based simulation of hydrogel in 3D bioprinting, there are fundamental differences between their work and our study. They used IPS IBOFlow software without proposing a numerical scheme for solving their model's equations. In contrast, we developed and implemented our own SPH method, providing full control over simulation parameters and enabling better tuning of the physical simulation to match real-world behaviour.

Unlike Göhl *et al* our Lagrangian-based SPH method is mesh-free, offering greater flexibility in handling complex geometry and deformations. Grid-based methods, employed by Göhl *et al* are limited by the initial mesh and are less adaptable for simulating spheroid fusion. Furthermore, they used an elastic-plastic model for the bioink, while our study utilizes an elastic-plastic model to simulate spheroid diffusion, capturing non-reversible deformations.

Compared to similar studies, the most important advantage of the present study is the use of a general framework that has high flexibility in simulating the behaviour of spheroids during fusion. Although visco-elastic differential equations have been used in the study of Beaune *et al* [60] and Ongenae *et al* [61], however, the fundamental difference in their solution method is an advantage for this research. First, the solution method presented in this paper is not dependent on the mesh. In other words, the Lagrangian approach is used to solve the model's differential equations, in which there is no need to discretize the spherical mesh. Therefore, our approach offers several advantages over the studies mentioned above for solving continuum mechanics differential equations: (i) Flexibility in domain representation: Since we are using meshless methods, we do not require a predefined mesh structure, allowing for a more flexible and adaptive representation of complex domains with irregular geometries. This makes our methods particularly suitable for problems involving free surfaces like deformations with changing topologies. (ii) Easy handling of moving boundaries: our method excels in handling problems with moving boundaries or interfaces. Since the computational particles used in our methods can easily be repositioned, tracking and handling moving boundaries becomes more straightforward than mesh-based methods requiring mesh regeneration or remeshing. (iii) Reduced computational cost: our method often exhibits computational efficiency advantages for problems with large deformations or when high accuracy is required. It does not suffer from the mesh distortion issues typically encountered in mesh-based methods, reducing computational effort associated with mesh updates or element distortion. (iv) Adaptive refinement: our method can achieve adaptive refinement by locally increasing the density of computational particles in regions where high accuracy is needed. This adaptivity allows for efficient concentration of computational effort in areas of interest without the need for global mesh refinement. (v) Natural treatment of discontinuities: our method naturally handles problems involving discontinuities, such as the fusion of spheroids. By placing computational particles near the discontinuities, accurate representation and modelling of these features can be achieved without the need for special treatments or complex mesh configurations. (vi) Last but not least is generality: our proposed framework is general. It means that it can simulate more than just two spheroids fusion, as it is shown in figure 4.

Ongenae *et al* [61] research has explored the concept of 'arrested coalescence,' where certain factors hinder the complete fusion of spheroids or droplets. Unlike Ongenae *et al* [61], who model arrested coalescence with a jamming effect in viscous

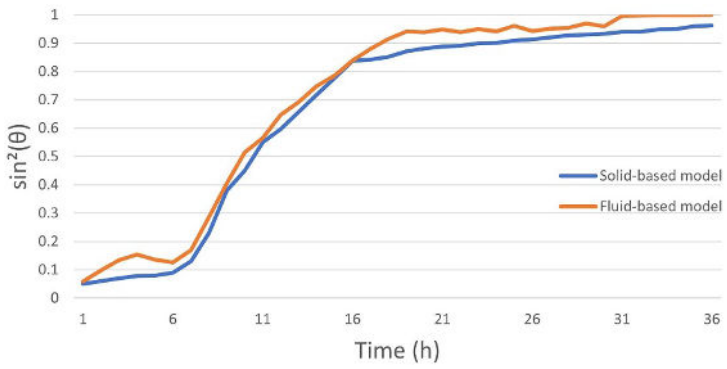

Figure 22. The values of $\sin^2(\theta)$ for solid-based and fluid-based models.

models, our general framework accommodates both solid and fluid states. The degree of fusion in our model is determined by specific parameters, such as stiffness, volume constant, internal pressure, Poisson ratio, and Young's modulus of particles. In summary, arrested coalescence in our paper is modelled as balanced between internal and external forces. Internal forces are elastic-plastic, volume conservation, pressure and viscosity and external force is the gravitational force between spheroids.

A significant difference in our approach lies in the method of force generation. Ongenae *et al* [61] primarily rely on geometric forces arising from changes in distances and contact angles between cells and spheroids. In contrast, our approach is rooted in inherent material properties, such as elasticity and plasticity, and derives forces from physical equations representing chemical interactions resulting from these properties. Considering material properties as the root cause of fusion and deformation in spheroids can better link the chemistry and biology of such a complex phenomenon to physics.

More in detail, while Ongenae *et al* [61] focuses on geometric forces and considers spheroids as perfect spheres, we simulate various deformations during fusion through our algorithm, considering particle positions on the spheroid surface. Our approach ensures that geometry and final shape are dictated by physics, taking into account elastic-plastic forces and volume conservation in solid-based models and pressure and viscosity forces in fluid-based models. Considering the material properties gives us the ability to control the geometry of the spheroids by tuning the current properties, such as stiffness or using different materials. While in Ongenae *et al* [61] paper, we do not have the ability to control the fusion process.

However, To quantitatively compare our presented model with the research of Ongenae *et al* [61], we conducted an analysis of two variables from their work. The first variable, denoted as $\sin^2(\theta) = (\frac{x}{a})^2$, where x is the length of contact area, and a is the spheroid's radius. θ is the contact angle, and $\sin^2(\theta)$ captures the dynamics of fusion according to Ongenae *et al* [61]. Figure 22 illustrates the fusion dynamics for solid and fluid-based models of our approach. In both cases, fusion initiates gradually with a small increase in the theta angle, indicating a low attraction force between the spheroids. However, as a bond is established between the spheroid particles, the fusion process accelerates until the gravitational force achieves equilibrium with internal forces, resulting in stable fusion. This observation contrasts with Ongenae *et al* [61], where fusion starts rapidly and continues at high speed until reaching equilibrium in figures 3(B) and 4(A). This discrepancy arises from the different definitions of gravity and internal forces in their model and ours. We believe that a gradual fusion rate at the start and end of the process aligns more naturally with our observations from *in-vitro* data. Unlike the model proposed by Ongenae *et al* [61], in our model, fast fusion is hindered by elastic collision and viscosity at the beginning. However, as we update the neighbours of each particle, bonds between particles of two spheroids form, accelerating fusion. This exemplifies the advantage of employing forces derived from material properties.

The second variable is the density of the entire system, which represents the average density of all particles contained with the two spheroids, plotted against a 36-hour fusion time. To compare the average density values for each model, we focused on the most important parameters of our model, namely Young's modulus, Poisson's ratio, fluid stiffness, and viscosity, as they significantly influence this variable.

Figure 23 displays the average density of spheroids over time for various values of Young's modulus, Poisson's ratio, stiffness, and viscosity. All four graphs exhibit similar trends, with increasing density as the fusion progresses. Specifically, in the fluid model, increasing stiffness and viscosity lead to an S-shaped behaviour in the density graph, where density initially increases and then decreases towards the end. This behaviour is attributed to the rise in fluid stiffness, which elevates internal pressure, resulting

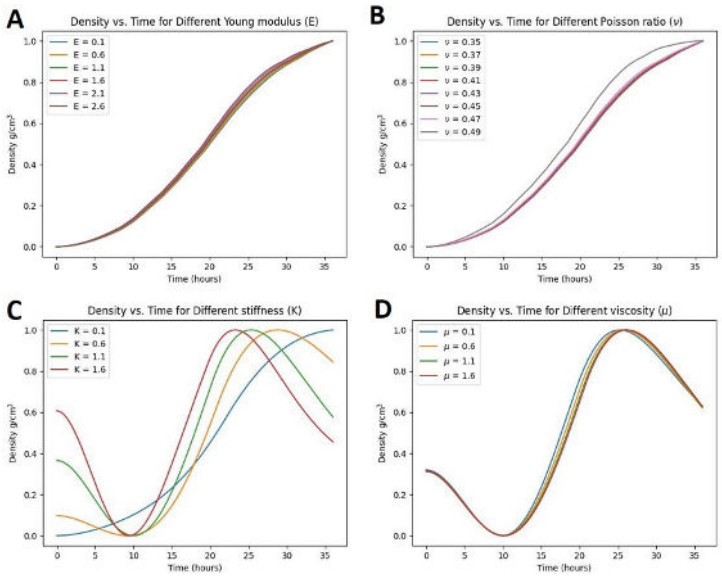

Figure 23. (A) Average density vs time for different Young's modulus. (B) Average density vs time for different Poisson ratio. (C) Average density vs time for different fluid stiffness. (D) Average density vs time for different fluid viscosity.

in increased volume and, consequently, decreased density. Comparing our results with figure 3. A of Ongenae *et al* [61] article reveals similar density trends during the fusion process, which is reasonable as we expect an increase in density when two spheroids are fused. Our approach adeptly captures arrested coalescence without relying on the 'jamming effect'. Instead, we leverage the intrinsic material properties of the spheroids to create internal forces that balance the gravitational force between them, resulting in the termination of fusion. This method is not only more realistic and versatile but also highly effective in modelling various types of behaviour beyond arrested coalescence. We regenerated the parameters that Ongenae *et al* [61] utilized in their study, which explicitly outline fusion dynamics as detailed in their paper and compared them with the result of [61]. The primary advantage of our approach lies in its ability to not only capture arrested coalescence with similar properties (as demonstrated in the density graph) but also to model various other fusion phenomena, including different types of deformation. This introduces a novel perspective to modelling spheroid fusion. In our case, we are capable of modelling fusion based on material properties rather than solely the geometry of the spheroids. This ability implies the potential for controlling the fusion process using diverse biological materials.

For future studies, to enhance the accuracy and relevance of our simulation and better align it with *in-vivo* experiments, it is important to consider additional factors, such as the inclusion of the hydrogel medium and the composition of the extracellular matrix (ECM). The ECM composition in fibroblasts, myocytes, and coronary cells plays a vital role in tissue structure and function, with fibroblasts producing collagen, fibronectin, and proteoglycans, myocytes interacting with collagen, laminins, and elastin, and coronary cells interacting with collagens, proteoglycans, and glycoproteins. The ECM provides structural support, regulates cell adhesion and migration, and contributes to tissue integrity. However, further investigation is needed to understand the specific ECM composition and its impact on spheroid fusion. Developing a fluid model that can accurately simulate the properties of the hydrogel and incorporate boundary conditions influenced by the ECM can be the subject of our future research.

6. Conclusion

This paper presents two continuum models for 3D bioprinted spheroids, addressing their movement during fusion to achieve desired tissue shapes and dimensions. We propose a physically-based simulation using SPH to model the spontaneous fusion process of spheroids. Initially, we consider spheroids as elastic-plastic solid materials, incorporating a volume conservation force to prevent excessive volume changes and high plastic deformation. Based on our observations, we develop a fluid-based model to simulate additional spheroid behaviours, such as viscous fluids with plastic deformation. Our study employs a physically-based simulation method for tissue formation in 3D bioprinting. The proposed framework is flexible, allowing for the simulation of various types of fusion and proving to be effective compared to *in-vitro* validation. Morphological analysis demonstrates that *in-silico* simulations and *in-vitro* data are not significantly different. However, we acknowledge that there are still open questions to be addressed. Thalheim *et al* [62] emphasize the

importance of establishing a link between *in-silico* parameters and *in-vitro* data, and they call for more clinical studies in this field. Our observations indicate that gaining a deeper understanding of the biological basis of spheroid fusion can lead us to more efficient physical models. Additionally, using machine learning to optimize and tune the model's parameters for creating tissue with the desired shape and real-time control of 3D bioprinting presents an interesting topic for future research.

Data availability statement

All data that support the findings of this study are included within the article (and any supplementary files).

Acknowledgment

The authors would like to acknowledge the support of the University of Sydney (Cardiothoracic Surgery Research Grant), UTS (Seed Funding), and the Catholic Archdiocese of Sydney (Grant for Adult Stem Cell Research) to C G. Thanks to Lydia Surija for providing cardiac spheroid images from the Gentile Lab.

ORCID iDs

Hassan Bahrami https://orcid.org/0000-0002-2925-2354
Enrico Puppo https://orcid.org/0000-0001-9780-5283
Stuart Perry https://orcid.org/0000-0002-2794-3178
Carmine Gentile https://orcid.org/0000-0002-3689-4275
Nico Pietroni https://orcid.org/0000-0002-8271-2102

References

[1] Zuppinger C 2019 Measurement of Contractility and Calcium Release in Cardiac Spheroids *Calcium-Binding Proteins of the EF-Hand Superfamily* (Springer) pp 41–52
[2] Gao L *et al* 2018 Large cardiac muscle patches engineered from human induced-pluripotent stem cell–derived cardiac cells improve recovery from myocardial infarction in swine *Circulation* **137** 1712–30
[3] Mattapally S, Zhu W, Fast V G, Gao L, Worley C, Kannappan R, Borovjagin A V and Zhang J 2018 Spheroids of cardiomyocytes derived from human-induced pluripotent stem cells improve recovery from myocardial injury in mice *Am. J. Physiol. Heart. Circ. Physiol.* **315** H327–39
[4] Mawad D, Figtree G and Gentile C 2017 Current technologies based on the knowledge of the stem cells microenvironments *Stem Cell Microenvironments and Beyond* pp 245–62 (available at: https://link.springer.com/chapter/10.1007/978-3-319-69194-7_13)
[5] Reis R 2019 *Encyclopedia of Tissue Engineering and Regenerative Medicine* (Academic)
[6] Polonchuk L, Chabria M, Badi L, Hoflack J-C, Figtree G, Davies M J and Gentile C 2017 Cardiac spheroids as promising *in vitro* models to study the human heart microenvironment *Sci. Rep.* **7** 1–12
[7] Polonchuk L and Gentile C 2021 Current state and future of 3d bioprinted models for cardio-vascular research and drug development *ADMET DMPK* **9** 231–42
[8] Visconti R P, Kasyanov V, Gentile C, Zhang J, Markwald R R and Mironov V 2010 Towards organ printing: engineering an intra-organ branched vascular tree *Expert Opin. Biol. Ther.* **10** 409–20
[9] Gentile C 2016 Filling the gaps between the *in vivo* and *in vitro* microenvironment: engineering of spheroids for stem cell technology *Curr. Stem Cell Res. Ther.* **11** 652–65
[10] Mironov V, Visconti R P, Kasyanov V, Forgacs G, Drake C J and Markwald R R 2009 Organ printing: tissue spheroids as building blocks *Biomaterials* **30** 2164–74
[11] Fleming P A, Argraves W S, Gentile C, Neagu A, Forgacs G and Drake C J 2010 Fusion of uniluminal vascular spheroids: a model for assembly of blood vessels *Dev. Dyn.* **239** 398–406
[12] Sharma P, Ming C L C, Wang X, Bienvenu L A, Beck D, Figtree G, Boyle A and Gentile C 2022 Biofabrication of advanced *in vitro* 3d models to study ischaemic and doxorubicin-induced myocardial damage *Biofabrication* **14** 025003
[13] Murphy S V, De Coppi P and Atala A 2020 Opportunities and challenges of translational 3d bioprinting *Nat. Biomed. Eng.* **4** 370–80
[14] Roche C D, Brereton R J, Ashton A W, Jackson C and Gentile C 2020 Current challenges in three-dimensional bioprinting heart tissues for cardiac surgery *Eur. J. Cardio-Thoracic Surg.* **58** 500–10
[15] Derakhshanfar S, Mbeleck R, Xu K, Zhang X, Zhong W and Xing M 2018 3d bioprinting for biomedical devices and tissue engineering: a review of recent trends and advances *Bioactive materials* **3** 144–56
[16] Groll J *et al* 2016 Biofabrication: reappraising the definition of an evolving field *Biofabrication* **8** 013001
[17] Groll J *et al* 2018 A definition of bioinks and their distinction from biomaterial inks *Biofabrication* **11** 013001
[18] Polonchuk L *et al* 2021 Towards engineering heart tissues from bioprinted cardiac spheroids *Biofabrication* **13** 045009
[19] Roche C D, Sharma P, Ashton A W, Jackson C, Xue M and Gentile C 2021 Printability, durability, contractility and vascular network formation in 3d bioprinted cardiac endothelial cells using alginate–gelatin hydrogels *Front. Bioeng. Biotechnol.* **9** 636257
[20] Campbell M, Chabria M, Figtree G A, Polonchuk L and Gentile C 2018 *Stem Cell-Derived Cardiac Spheroids as 3d in Vitro Models of the Human Heart Microenvironment* (Springer) pp 51–59
[21] Forgacs G, Foty R A, Shafrir Y and Steinberg M S 1998 Viscoelastic properties of living embryonic tissues: a quantitative study *Biophys. J.* **74** 2227–34
[22] Kim S-J, Byun H, Lee S, Kim E, Lee G M, Huh S J, Joo J and Shin H 2022 Spatially arranged encapsulation of stem cell spheroids within hydrogels for the regulation of spheroid fusion and cell migration *Acta Biomater.* **142** 60–72
[23] Li J, Wu C, Chu P K and Gelinsky M 2020 3D printing of hydrogels: rational design strategies and emerging biomedical applications *Mater. Sci. Eng.* R **140** 100543
[24] Foty R A and Steinberg M S 2005 The differential adhesion hypothesis: a direct evaluation *Dev. Biol.* **278** 255–63
[25] Wadkin L, Orozco-Fuentes S, Neganova I, Lako M, Shukurov A and Parker N 2020 The recent advances in the mathematical modelling of human pluripotent stem cells *SN Appl. Sci.* **2** 276
[26] Ghaffarizadeh A, Heiland R, Friedman S H, Mumenthaler S M and Macklin P 2018 Physicell: an open source physics-based cell simulator for 3-d multicellular systems *PLoS Comput. Biol.* **14** e1005991
[27] Göhl J, Markstedt K, Mark A, Håkansson K, Gatenholm P and Edelvik F 2018 Simulations of 3D bioprinting: predicting bioprintability of nanofibrillar inks *Biofabrication* **10** 034105

[28] Bonatti A F, Chiesa I, Vozzi G and De Maria C 2021 Open-source cad-cam simulator of the extrusion-based bioprinting process *Bioprinting* **24** e00172
[29] Ramezani H, Mohammad Mirjamali S and He Y 2022 Simulations of extrusion 3d printing of chitosan hydrogels *Appl. Sci.* **12** 7530
[30] Müller M, Keiser R, Nealen A, Pauly M, Gross M and Alexa M 2004 Point based animation of elastic, plastic and melting objects *Proc. 2004 ACM SIGGRAPH/Eurographics Symposium on Computer Animation* pp 141–51
[31] Witkin A 2001 Physically Based Modeling Particle System Dynamics *ACM SIGGRAPH Course Notes*
[32] Nealen A, Müller M, Keiser R, Boxerman E and Carlson M 2006 Physically Based deformable models in computer graphics *Computer Graphics Forum* vol 25 (Wiley) pp 809–36
[33] Baraff D 2001 Physically based modeling: rigid body simulation *SIGGRAPH Course Notes, ACM SIGGRAPH 2* 2–1
[34] Muller M, Teschner M and Gross M 2004 Physically-based simulation of objects represented by surface meshes *Proc. Computer Graphics Int., 2004* (IEEE) pp 26–33
[35] Costa I F and Balaniuk R 2001 Lem-an approach for real time physically based soft tissue simulation *Proc. 2001 ICRA. IEEE Int. Conf. on Robotics and Automation (Cat. No.01CH37164)* vol 3 (IEEE) pp 2337–43
[36] Wu J, Westermann R and Dick C 2015 A survey of physically based simulation of cuts in deformable bodies *Computer Graphics Forum* vol 34 (Wiley) pp 161–87
[37] Barbič J and Popović J 2008 Real-time control of physically based simulations using gentle forces *ACM Trans. Graph.* **27** 1–10
[38] Müller M, Bender J, Chentanez N and Macklin M 2016 A robust method to extract the rotational part of deformations *Proc. 9th Int. Conf. on Motion in Games* pp 55–60
[39] Nguyen D Q, Fedkiw R and Jensen H W 2002 Physically based modeling and animation of fire *Proc. 29th Annual Conference on Computer Graphics and Interactive Techniques* pp 721–8
[40] Liu S, Liu Q and Peng Q 2011 Realistic simulation of mixing fluids *Vis. Comput.* **27** 241–8
[41] Takahashi T, Dobashi Y, Fujishiro I, Nishita T and Lin M C 2015 Implicit formulation for sph-based viscous fluids *Computer Graphics Forum* vol 34 (Wiley) pp 493–502
[42] Macklin M, Müller M, Chentanez N and Kim T-Y 2014 Unified particle physics for real-time applications *ACM Trans. Graph.* **33** 1–12
[43] Cornelis J, Bender J, Gissler C, Ihmsen M and Teschner M 2019 An optimized source term formulation for incompressible sph *Vis. Comput.* **35** 579–90
[44] Ren B, Yang X-Y, Lin M C, Thuerey N, Teschner M and Li C 2018 Visual simulation of multiple fluids in computer graphics: A state-of-the-art report *J. Comput. Sci. Technol.* **33** 431–51
[45] Wang X, Ramírez-Hinestrosa S, Dobnikar J and Frenkel D 2020 The lennard-jones potential: when (not) to use it *Phys. Chem. Chem. Phys.* **22** 10624–33
[46] Iyer S S, Mazarakos K P and Zhou H-X 2022 Molecular dynamics simulations of droplet fusion reveals shear thinning *Biophys. J.* **121** 472a
[47] Walker C C, Genzer J and Santiso E E 2019 Development of a fused-sphere saft-γ mie force field for poly (vinyl alcohol) and poly (ethylene) *J. Chem. Phys.* **150** 034901
[48] Winograd-Katz S E, Fässler R, Geiger B and Legate K R 2014 The integrin adhesome: from genes and proteins to human disease *Nat. Rev. Mol. Cell Biol.* **15** 273–88
[49] Sun Z, Costell M and Fässler R 2019 Integrin activation by talin, kindlin and mechanical forces *Nat. Cell Biol.* **21** 25–31
[50] O'brien J F, Bargteil A W and Hodgins J K 2002 Graphical modeling and animation of ductile fracture *Proc. 29th Annual Conference on Computer Graphics and Interactive Techniques* pp 291–4
[51] Liu M and Liu G 2010 Smoothed particle hydrodynamics (sph): an overview and recent developments *Arch. Comput. Methods Eng.* **17** 25–76
[52] Israelachvili J N 2011 *Intermolecular and Surface Forces* (Academic)
[53] Berland K, Cooper V R, Lee K, Schröder E, Thonhauser T, Hyldgaard P and Lundqvist B I 2015 van der waals forces in density functional theory: a review of the vdw-df method *Rep. Prog. Phys.* **78** 066501
[54] Serway R A and Jewett J W 2018 *Physics for Scientists and Engineers* (Cengage learning)
[55] Museth K 2013 Vdb: High-resolution sparse volumes with dynamic topology *ACM Trans. Graph.* **32** 1–22
[56] Nielson G 2004 Dual marching cubes *IEEE Visualization 2004 - Proc., VIS 2004* pp 489–96
[57] Museth K, Budsberg J, Hankins R, Keeler T, Bailey D and Hoetzlein R 2017 Openvdb *ACM Siggraph 2017 Courses, Siggraph '17* (Association for Computing Machinery)
[58] Susienka M J, Wilks B T and Morgan J R 2016 Quantifying the kinetics and morphological changes of the fusion of spheroid building blocks *Biofabrication* **8** 045003
[59] Schindelin J *et al* 2012 Fiji: an open-source platform for biological-image analysis *Nat. Methods* **9** 676–82
[60] Beaune G, Sinkkonen L, Gonzalez-Rodriguez D, Timonen J V and Brochard-Wyart F 2022 Fusion dynamics of hybrid cell–microparticle aggregates: a jelly pearl model *Langmuir* **38** 5296–306
[61] Ongenae S, Cuvelier M, Vangheel J, Ramon H and Smeets B 2021 Activity-induced fluidization and arrested coalescence in fusion of cellular aggregates *Front. Phys.* **9** 649821
[62] Thalheim T, Aust G and Galle J 2022 Organoid cultures *in silico*: Tools or toys? *Bioengineering* **10** 50